Investigation of mechanical and electrical characteristics of self-sensing pneumatic torsional actuators

XIAO Wei[1*], HU DeAn[2], HU GuoLiang[1] & XIAO YiHua[1]

[1] *Key Laboratory of Conveyance and Equipment, Ministry of Education, East China Jiaotong University, Nanchang 330013, China;*
[2] *Key Laboratory of Advanced Design and Simulation Techniques for Special Equipment, Ministry of Education, Hunan University, Changsha 410082, China*

Soft pneumatic actuators are one of the most promising actuation for soft robots, and great achievements have been obtained. But it remains challenging to endow sensing capabilities to pneumatic actuators, especially for the sensing ability originating directly from the actuator architecture. Herein, a self-sensing pneumatic torsional actuator (SPTA) is designed based on the electromagnetic induction effect and magnetically responsive materials. The SPTA can generate feedback voltage and current with the deformation, in which the sensing function comes from its inherent structure. To investigate the mechanical and electrical characteristics, an experimental platform and a finite element model are established, respectively. We find that the torsion angle and output torque increase in nonlinear with the actuating pressure. The maximum torsion angle is 66.35°, which is 84.34% of that for the actuator fabricated by pure rubber. The maximum output torque (24.9 N mm) improves by 23.19% compared with the actuator made by pure rubber. As regards the electrical characteristics, the maximum feedback voltage and current are 2.90 µV and 29.50 nA when the SPTA is actuated by a pressure of −40 kPa. We also demonstrate that the relationship between the torsion angle and the magnetic flux change is approximately linear. Finally, the number of turns of wires, magnetic powders contents, and magnetic direction on the feedback voltage and current are studied. Results show that the feedback voltage and current can be enhanced by increasing the number of turns and magnetic powders contents. We envision that the SPTA would be promising for soft robots to realize their accuracy control and intelligentization.

pneumatic torsional actuators, self-sensing, feedback voltage, finite element modeling, soft robots

1 Introduction

Robots, as an effective tool to liberate the labor force, have always been a research hotspot in the engineering and scientific communities. Traditional rigid robots possessing high load capacity and control precision are widely applied to manufacturing processing, industrial production, medical rehabilitation, etc. [1–3]. However, poor compliance and adaptation heavily limit the further research and application of rigid robots. Recently, advances in materials science and manufacturing methods have boosted the research on soft robots [4]. To date, many soft robots with various actuation methods, such as external motors [5,6], thermal actuation [7,8], photostimulation [9], and highly compressed fluids [10–12]. Among these soft robots, ones actuated by compressed fluids (soft pneumatic robots) are the most attractive due to their low cost, simple fabrication, and easy control. They are successfully applied to robotic grasping [13,14], neuroprosthetic hand [15,16], and subsea operation [17,18].

Soft pneumatic actuators, which are the crucial parts of pneumatic robots, have been highly concerned and studied. With persistent efforts, a variety of soft pneumatic actuators

---

* Corresponding author (email: xiaoweiqq@ecjtu.edu.cn)

have been developed. They can generate elongation [19,20], contraction [21,22], bending [23–25], rotation [26,27], and torsion [28,29] motion upon pressurization or depressurization. A characteristic of most actuators is that they demonstrate different motions via simple open-loop control. Therefore, it is difficult for these actuators to realize accuracy control and actively interact with environments because of a lack of mechanical sensing abilities [30]. In nature, biologies can be viewed as an intelligent system that possesses the ability to motion, sense, and control. Thus, integrating sensors into soft pneumatic actuators is promising to extend their applications. At present, many soft sensors are proposed based on diverse sensing mechanisms, for example, resistance variation [31,32], capacitive effect [33,34], inductance sensing [35], photoelectric effect [36], etc. [37,38]. For instance, Kanno et al. [39] created a dielectric elastomer sensor and embedded it into McKibben artificial muscles, so the muscles can sense their elongitudinal displacement. Ying et al. [31] designed a highly stretchable ionic skin that was applied to pneumatic bending actuators to obtain reliable deformation feedback. Gu et al. [15] customized a capacitive sensor that was mounted onto the pneumatic bending fingers. Besides, many attempts have been made to integrate soft sensors into soft actuators [40–42]. But there are still many difficulties and challenges in employing the sensors in soft pneumatic actuators. Firstly, the integration of such sensors into soft actuators requires sophisticated fabrication processes and dedicated setups, which causes production to be laborious and costly [43]. The integration and arrangement of sensing elements also need to be considered in practical applications. Ideally, the sensing ability should originate from the actuator architecture [44]. In addition, most of the available research mainly focuses on the sensing of the elongating/contracting and bending actuators. Since the torsion motion is relatively complicated, there are very few studies on the sensing of torsional actuators. Therefore, developing a novel pneumatic torsional actuator with simple fabrication and inherent sensing ability is significant work for soft robots.

As we know, the electromagnetic induction effect was first observed by Michael Faraday [45], which opens the door for converting mechanical energy into electrical energy. Electromagnetic generators are one of the most successful applications of the electromagnetic induction effect. Recently, magnetically responsive materials have been fabricated through incorporating magnetic particles into silicone rubber [46,47]. The composite material is completely soft and magnetic after magnetizing. If the hard magnet of electromagnetic generators is replaced with the composite material, the generators can also produce an induced voltage as the composite material moves or deforms. This provides a new approach to developing self-sensing pneumatic actuators.

To achieve this idea, we design a self-sensing pneumatic torsional actuator (SPTA) that can feel its deformation. The sensing function comes from the inherent structure of the actuator without integrating additional sensors. And the SPTA can be fabricated easily by multi-step casting methods, where the composite materials were poured into the molds containing a helical varnished wire. In this paper, the overall design, sensing principle, and fabrication are detailed first. To investigate the mechanical characteristics of the SPTA, a finite element model is established and validated experimentally. In addition, experiments are carried out in order to reveal the electrical characteristics of the SPTA and the relationship between the torsion deformation and the magnetic flux change. Finally, the effect of three main factors, including the number of turns of the varnished wire, magnetic powders contents, and magnetic direction, on the feedback voltage and current is studied, respectively.

2 Materials and methods

2.1 Overall design and sensing principle

The design of the self-sensing pneumatic torsional actuator (SPTA) is shown in Figure 1(a) and (b). The SPTA mainly consists of an elastomeric body and a helical varnished wire placed in the center of the SPTA. The elastomeric body possesses four helical chambers with an elliptical section (The semi-axes of the elliptical section are 5 and 4 mm). All the chambers are connected to a common air inlet and outlet. When negative pressure is applied to the chambers, the chamber will collapse cooperatively, resulting in the torsion deformation of the top end. More details about the structure and the torsion mechanism can be found in our earlier work [48]. Different from the existing pneumatic torsional actuator [29,48], the elastomeric body is made of a silicone rubber/ NdFeB composite rather than pure silicone rubber. The composite is completely soft and magnetic after magnetization. The mechanical softness and magnetism of the composite are the preconditions to realize the self-sensing of pneumatic torsional actuators. Additionally, the varnished wire is the prominent characteristic of the SPTA. The varnished wire with a diameter of 0.2 mm is designed as helical structures (diameter of 4 mm, height of 32 mm, 50 turns), which allows them to deform or recover easily as the torsional actuator is twisting or recovering.

For our proposed SPTA, the elastomeric body will generate a local magnetic field around, which yields magnetic flux passing through the helical varnished wire (Figure 1(c)). When the SPTA is actuated by negative pressures, the magnetic intensity distribution will change accompanied by the deformation of the elastomeric body. Consequently, the magnetic flux passing through each turn of varnished wires will alter in the meantime. Based on Faraday's electromagnetic induction laws, the variation of magnetic flux in
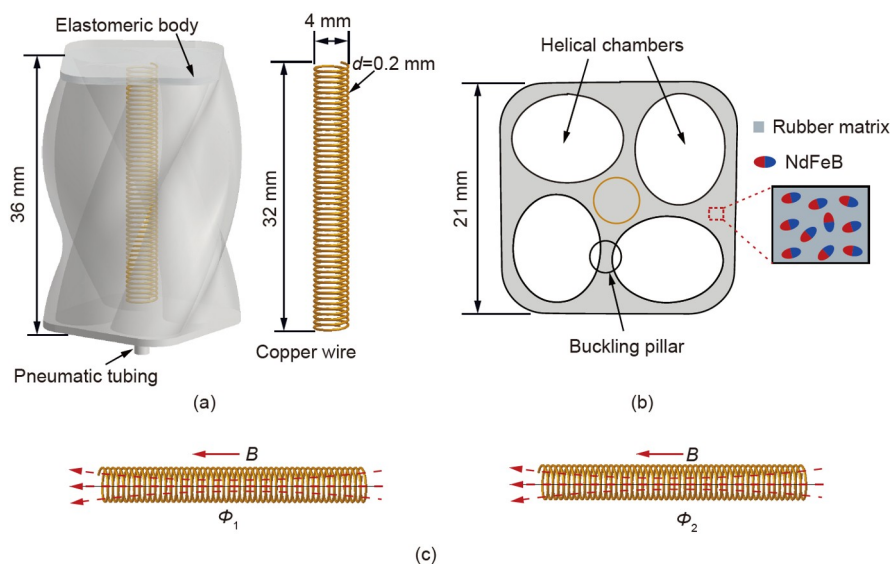
Figure 1   (Color online) Overall design and sensing principle of the STPA. (a) Schematic illustration of the STPA; (b) cross section of the STPA; (c) magnetic flux passing through each turn of varnished wires for initial and twisting status.

the wire is able to produce induced voltages, which can be expressed as follows:

$$E(v) = -N \cdot \frac{\Phi_2 - \Phi_1}{\Delta t}, \tag{1}$$

where $E(v)$ is the induced voltage, N is the number of turns of varnished wires, Φ_1 and Φ_2 are the magnetic flux passing through each turn of varnished wires for initial and twisting status, respectively, Δt is the time span corresponding to the change of the magnetic flux.

2.2   Fabrication of the SPTA

The multi-step casting approach is employed to fabricate the SPTA. Before fabricating the SPTA, the molds for casting were printed with the material SOMOS Imagine 8000. Compared with the pneumatic torsional actuator [48], there are three differences during the fabrication process. Firstly, the soft material of silicone rubber is replaced by the silicone rubber/NdFeB composite. Thus, the silicone rubber/NdFeB composite needs to be prepared prior to casting. Two components of silicone rubber (E625, Hong Ye Jie) with the same mass are taken out and then poured into a beaker. At the same time, the NdFeB magnetic powders (LW-N-11-9, Xinnuode, mean diameter of 37 μm) with the same weight as the silicone rubber are also added to the beaker. The mixture will be stirred via a blender for about 3–5 min to obtain the homogeneous composite. In our previous work [49], experiments of the cross-sectional SEM for the silicone rubber/NdFeB composite are performed. Based on the cross-sectional SEM images, we find that the magnetic powders are dispersed uniformly in the silicone rubber matrix as the mass fractions of magnetic powders vary from 30% to 70%. Secondly, a helical varnished wire is embedded into the elastomeric body

to generate the voltage signal. Therefore, the helical varnished wire should be fabricated and placed into the assembled molds. Thirdly, the cured SPTA is magnetized to saturation via a commercial magnetizer (PFD-2000, Tianjie), where the applied impulse field is about 3.25 T. Other than these, the fabrication process is the same as the pneumatic torsional actuator, which can be found in ref. [48]. The finished SPTA is displayed in Figure 2(a). For the sake of experiments, two cubical silicone rubber (with the dimensions of 10 mm×10 mm×10 mm) are glued on the top and bottom of the SPTA, respectively.

2.3   Methods for the characteristic tests

For the SPTA, it will generate torsion deformation and electrical signal (voltage and current) under the actuation of negative pressures. Here, experimental platforms were con-
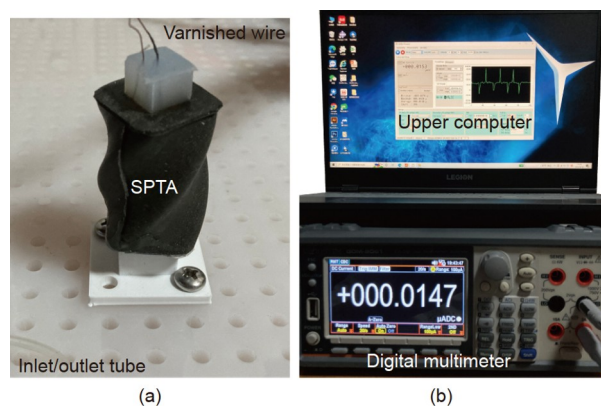

Figure 2   (Color online) Experimental platform for measuring the feedback electrical signal of the SPTA. (a) Image of SPTA, where its end is fixed in a platform; (b) digital multimeter and upper computer.

structed to investigate the mechanical and electrical characteristics. Firstly, the torsion angle and the output torque were measured. The experimental setup mainly contains a pressure control and output system, torsion angle, and output torque measurement platform, which is detailed in our previous work [48]. In addition, a measurement platform was established to measure the electrical signal, as demonstrated in Figure 2. The platform chiefly includes a multimeter and an upper computer. The multimeter (Good Will Instrument Co., Ltd. GDM-8261A) is six bit semi, dual-display digital multimeter. The basic accuracy is 0.0035%, and the resolution ratio of voltage is 0.1 μV, while the resolution ratio of current is 100 pA. For the SPTA, the feedback voltage and current are about a few microvolts and tens of microamps, respectively. From the point of view of accuracy and resolution, the multimeter we choose can meet the accuracy requirements. The SPTA was placed in a platform and its end was fixed. The two ends of the varnished wire were connected to the input port of the multimeter. Then, the feedback signal can be detected by the multimeter and transmitted to the upper computer. The collected signals were saved and displayed by the upper computer in real-time.

2.4   Finite element modeling

Prior to finite element modeling, the uniaxial tensile test is conducted to explore the material behavior of the silicone rubber/NdFeB composite. According to the standard ISO 37, the dumbbell-shaped specimen was fabricated and tested. The strain is equal to the crosshead displacement divided by the initial length of the specimen, while the stress is obtained by the ratio of the applied force to the cross-section area of the specimen. The stress-strain curve of the composite is shown in Figure 3. Herein, a reduced 2-order polynomial hyperelastic model is employed to simulate the material behavior of the silicone rubber/NdFeB composite. Its strain energy function can be written as follows [50]:

$$U = \sum_{i=1}^{2} C_{i0}(I_1 - 3)^i, \tag{2}$$

where I_1 denotes the first deviatoric strain invariant, C_{i0} represents the material coefficient. Then the stress-strain data were imported into ABAQUS to fit the material coefficients. The material coefficients of the silicone rubber/NdFeB composite are: C_{10}=0.1314 MPa, C_{20}=0.0073 MPa.

To model the deformation behavior of the SPTA, a 3D finite element model (FEM) was established by employing the software Abaqus/Explicit (Simulia, Dassault Systemes). Firstly, the geometrical model of the SPTA is imported to Abaqus, in which the inlet/outlet for pressurized air is ignored for simplifying the FEM. The elastomeric body of the SPTA is modeled using solid tetrahedral quadratic modified elements. For the helical varnished wire, quadratic beam
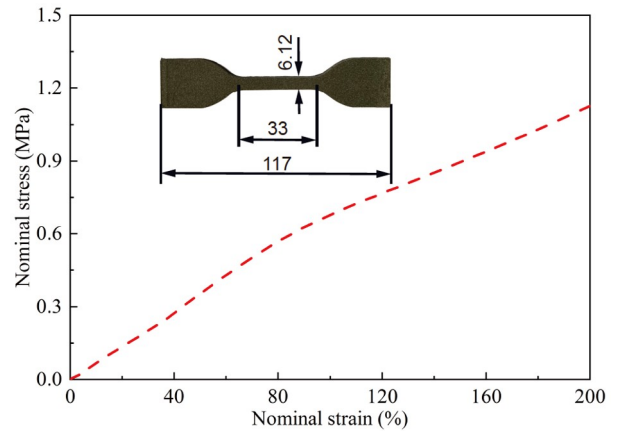

Figure 3   (Color online) Stress-strain curves of experimental data and dumbbell-shaped specimen for the silicone rubber/NdFeB composite.

elements (Abaqus element type B32) are used, which are connected to the elastomeric body by embedded constraints. The material of the helical varnished wire is modeled as linear elastic (Young's modulus of E=108000 MPa and Poisson's ratio of v=0.326). Four helical chambers of the elastomeric body are subjected to a uniformly distributed negative pressure. The bottom of the SPTA is completely fixed while the top is free. To avoid the penetration of chambers, the general contact in ABAQUS is also employed. The tangential contact behavior between the chambers is simulated by using the penalty method with a friction coefficient of 0.3, and the normal contact behavior is viewed as "hard" contact allowing separation after contact. Note that the measurement of the torsion angle is a static process. To be consistent with the experiment, the quasi-static conditions were guaranteed in the FEM via controlling the kinetic energy that should be less than 5% of the internal energy. When the actuating pressure of −40 kPa is applied to the chambers, the deformation of the SPTA and the helical varnished wire is demonstrated in Figure 4. In addition, the output torque can be also modeled. In the FEM, the top end of the SPTA is constrained by coupled with a reference point. The output torque of the SPTA is equal to the reaction torque of the reference point.

3   Results

3.1   Mechanical characteristics of the SPTA

According to numerical and experimental methods, the mechanical characteristics of the SPTA can be investigated thoroughly. Firstly, the torsion angle and output torque are measured based on the experimental platform that can be seen in our early work [29]. To obtain a more reasonable result, we have prepared two samples of the SPTA for the tests. Each sample will be measured twice to minimize the
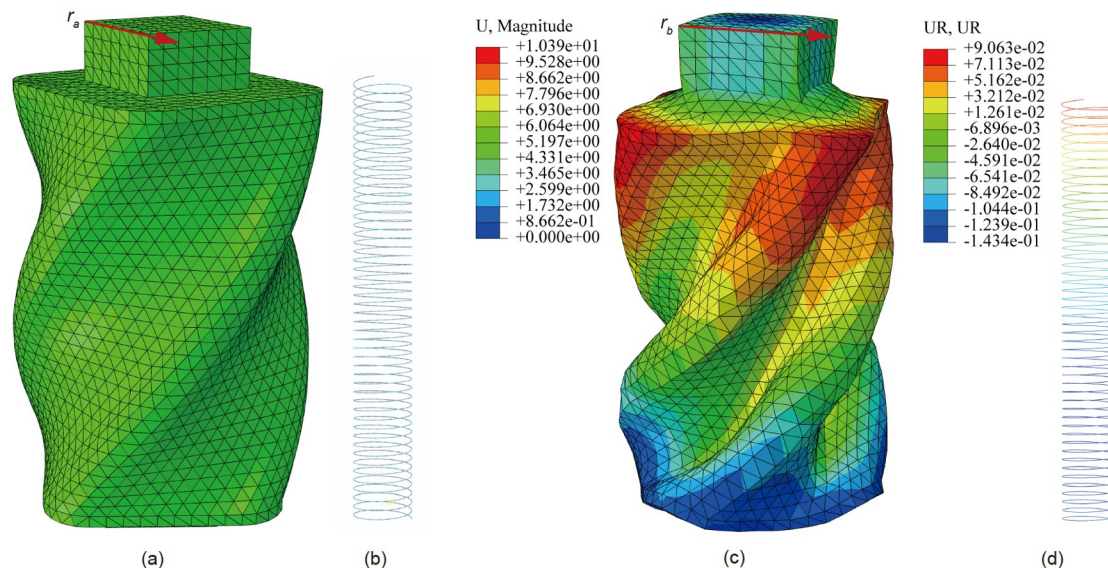
Figure 4   (Color online) Finite element analysis of the SPTA. (a) FEM of the SPTA; (b) mesh of the helical varnished wire; (c) deformation of the SPTA; (d) the helical varnished wire when the actuating pressure of −40 kPa is applied to the chambers.

experimental error. Figure 5 demonstrates the experimental results of the torsion angle and output torque for the SPTA. The relationship between the actuating pressure and the torsion angle is nonlinear. The increase in actuating pressures will lead to the rise of the torsion angle. The variation of torsion angle is minor as the actuating pressure exceeds −20 kPa. The torsion angle of the SPTA is 66.35° when the actuating pressure is −45 kPa. As regards the output torque, it increases nonlinearly with the actuating pressure. The output torque reaches a maximum (24.9 N mm) when the actuating pressure is −40 kPa. In addition, the torsion angle and output torque of the SPTA are also studied numerically, and the results are displayed in Figure 5. The match of the numerical and experimental results is good on the whole. The relative error of the maximum torsion angle and output torque between the FEM results and experiment results is less than 2%. On the other hand, some deviations exist under the small actuating pressure. This is due to the pressure loss caused by the elastic tubes during the experiment. And the deviation of the material model employed in the FEM also results in the discrepancies between the FEM results and experimental results. In short, the developed FEM is effective in predicting the mechanical characteristics of the SPTA.

Based on the developed FEM, we reveal the effect of the NdFeB magnetic powders and the helical varnished wire on the torsional performance. The torsional actuator fabricated by the pure rubber E625, E625/NdFeB, and E625/NdFeB and embedded helical varnished wire (SPTA) is simulated, respectively. The torsion angle and output torque of the torsional actuators are shown in Figure 6. There is a slight difference in torsion angle for the actuators with different materials (E625, E625/NdFeB). Whereas, the helical varn-

ished wire will reduce the torsion angle of torsional actuators. Compared with the torsional actuator fabricated by E625/NdFeB, the torsion angle of SPTA decreases by 15.66% when the actuating pressure is −45 kPa. On the other hand, the addition of NdFeB magnetic powders and helical varnished wire will enhance the output torque of torsional actuators. Compared with the actuator fabricated by E625, the maximum output torque for E625/NdFeB increases by 15.68% while the maximum output torque for SPTA improves by 23.19%.

In addition, the stiffness of the actuator for different materials is calculated and discussed. The generalized stiffness K is defined as the ratio of the actuating pressure and the torsion angle of the actuator, which can be expressed as

$$K = \frac{P_i}{\theta_i}, \tag{3}$$

where θ_i represents the torsion angle corresponding to the applied pressure P_i. Based on numerical data, the generalized stiffness of the actuator fabricated by the pure rubber E625, E625/NdFeB, and E625/NdFeB and embedded helical varnished wire (SPTA) is obtained. Here, the generalized stiffness (as the actuating pressure is −45 kPa) for the E625, E625/NdFeB, and SPTA is 32784.1, 33325.5, and 39521.4 Pa/rad, respectively. In conclusion, the NdFeB magnetic powders will increase the stiffness of the actuator, but the effect is small. The copper wires possess a stronger influence on the stiffness of the actuator.

In addition, the dynamic response of the SPTA is discussed. During the experiments, a camera is employed to record the dynamic response when the square signals with the pressure amplitude of −10, −20, −30, and −40 kPa are applied to the SPTA, respectively. The torsion angle of the
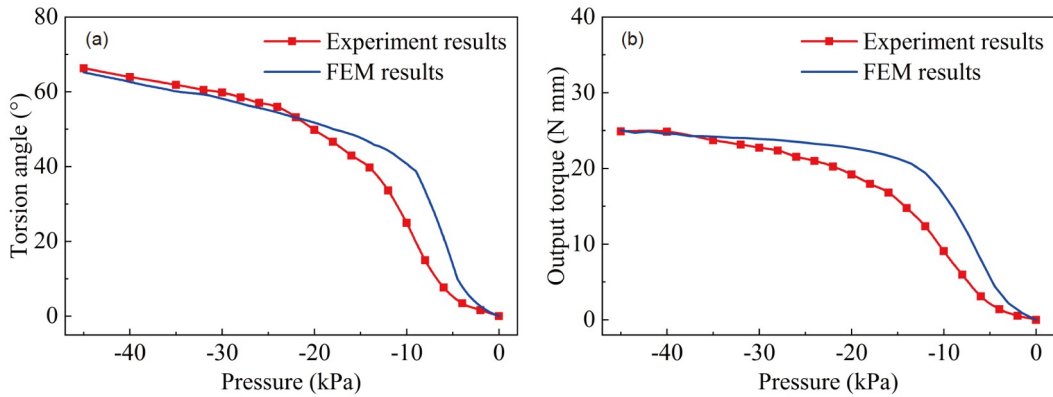
Figure 5 (Color online) Torsional performance of the SPTA. (a) Relationship between the torsion angle and the actuating pressure; (b) relationship between the output torque and the actuating pressure.
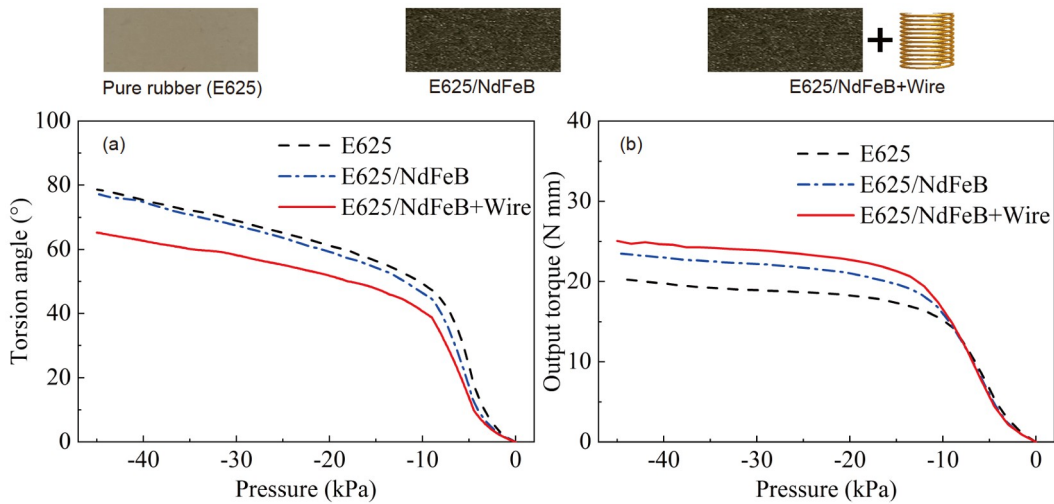

Figure 6 (Color online) Effect of the magnetic powder and varnished wire on the torsional performance of torsional actuators. (a) Torsion angle; (b) output torque.

SPTA is demonstrated in Figure 7. The maximum torsion angle of the SPTA increases with the pressure amplitude, and it is slightly bigger than the static measurement of the torsion angle. For the response time and recovery time, they are insensitive to the pressure amplitude. The average response time and recovery time are about 0.54 and 0.43 s, respectively.

3.2 Electrical characteristics of the SPTA

Accompanied by the torsion deformation, the SPTA will generate feedback voltage signals. Herein, the feedback voltage of the SPTA for different actuating pressures is investigated first. As detailed in Section 2.3, the feedback voltage is measured as a step pressure signal is applied to the SPTA, which can be found in Figure 8(a)–(d). Based on Faraday's electromagnetic induction laws, the induced voltage is equal to the ratio of the magnetic flux change and the time span. The rate of actuating pressures will affect the time span when the magnetic flux change remains constant.
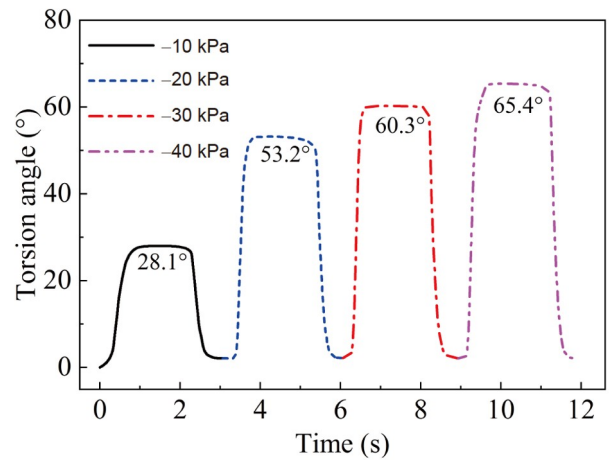

Figure 7 (Color online) Dynamic response of the torsion angle when different pressures are applied to the SPTA.

Therefore, the feedback voltage characterized in Figure 8 is related to the rate of actuating pressures. In our experiment, a step pressure signal is applied to the SPTA, which is con-
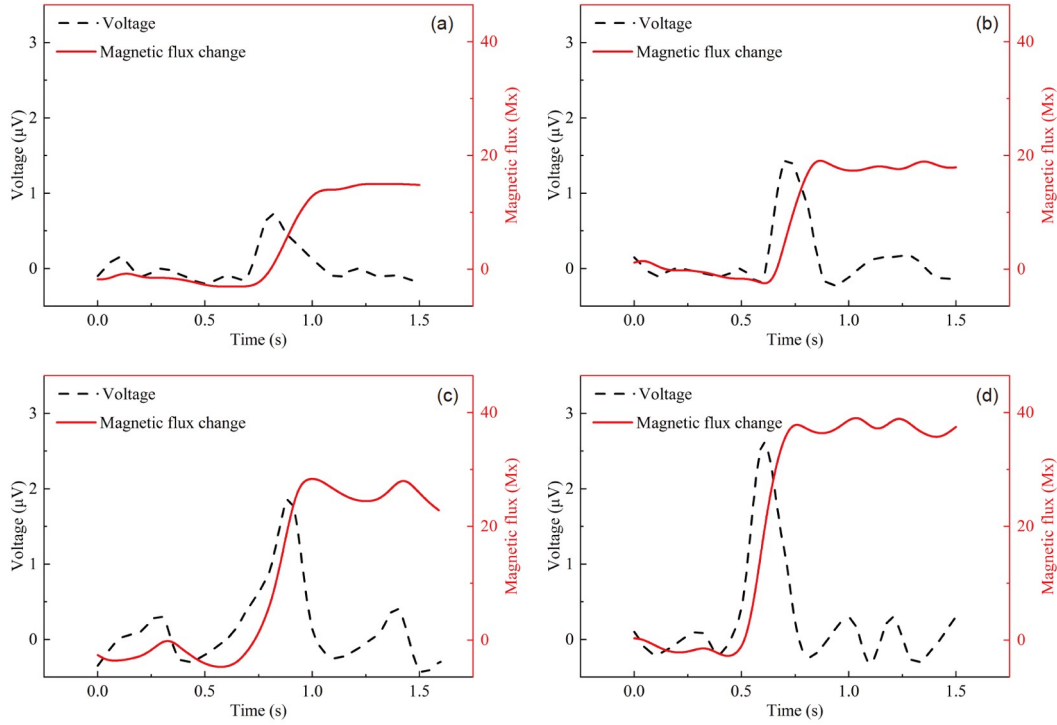
Figure 8   (Color online) Feedback voltage and magnetic flux change of the SPTA under the actuating pressures of (a) −10 kPa, (b) −20 kPa, (c) −30 kPa, and (d) −40 kPa.

trolled by using a solenoid valve. The rate of actuating pressures depends on the flow control valve. The rate of actuating pressures is unchanged during the measurement. In the voltage versus time curve, there is an obvious peak with a period of about 0.5 s that is close to the response time of the torsion angle. And the peak of the feedback voltage increases with the applied pressure. The maximum feedback voltages of the SPTA for different applied pressures of −10, −20, −30, and −40 kPa are about 0.70, 1.40, 1.85, and 2.60 µV, respectively. After the peak, there is a small oscillation in the voltage versus time curve owing to the effect of noise signals.

As we know, the feedback voltage of the SPTA is produced by the change in magnetic flux. Thus, we analyze the change of magnetic flux as well. The change of magnetic flux is obtained from the time integration of the feedback voltage, as expressed by the following:

$$\Delta \Phi = \int E(v) \mathrm{d}t. \tag{4}$$

Figure 8 demonstrates the change of magnetic flux versus time curves. The change of magnetic flux rises with time and then reaches a steady state. Due to the noise signal, the change of magnetic flux will oscillate within a small range during a steady state.

Obviously, the underlying cause of the change of magnetic flux is the torsion deformation of the SPTA. In this study, the torsion angle is used to describe the deformation of the

SPTA. We can find that the variation tendency of the change of magnetic flux and the torsion angle with respect to time is the same. But the quantitative relation between the torsion deformation and the change of magnetic flux is unclear so far. To disclose their underlying relationship, we plotted the magnetic flux change versus the torsion angle curve as the actuating pressures are −10, −20, −30, and −40 kPa, respectively. As shown in Figure 9, the magnetic flux change rises with the increase of the torsion angle. The magnetic flux change and the torsion angle exhibit a strong linear correlation, especially in the actuating state. Therefore, linear fitting is used to assess their quantitative relation. The fitting results are also demonstrated in Figure 9, which indicates excellent linearity for the magnetic flux change and the torsion angle. Furthermore, the coefficient of determination (R^2) is used to evaluate the overall accuracies of the linear fitting, which can be calculated by

$$R^2 = 1 - \frac{\sum_{i=1}^{u}(y_i - \tilde{y}_i)^2}{\sum_{i=1}^{u}(y_i - \overline{y}_i)^2}, \tag{5}$$

where u is the number of the experimental data, y_i and $\tilde{y}_i$ are the experimental result and the fitting result, respectively, $\overline{y}_i$ is the mean of the experimental result. The values of R^2 are 0.9803, 0.9787, 0.9883, and 0.9892 for the actuating pressures of −10, −20, −30, and −40 kPa. All the values are pretty close to 1, which further demonstrates their strong linear
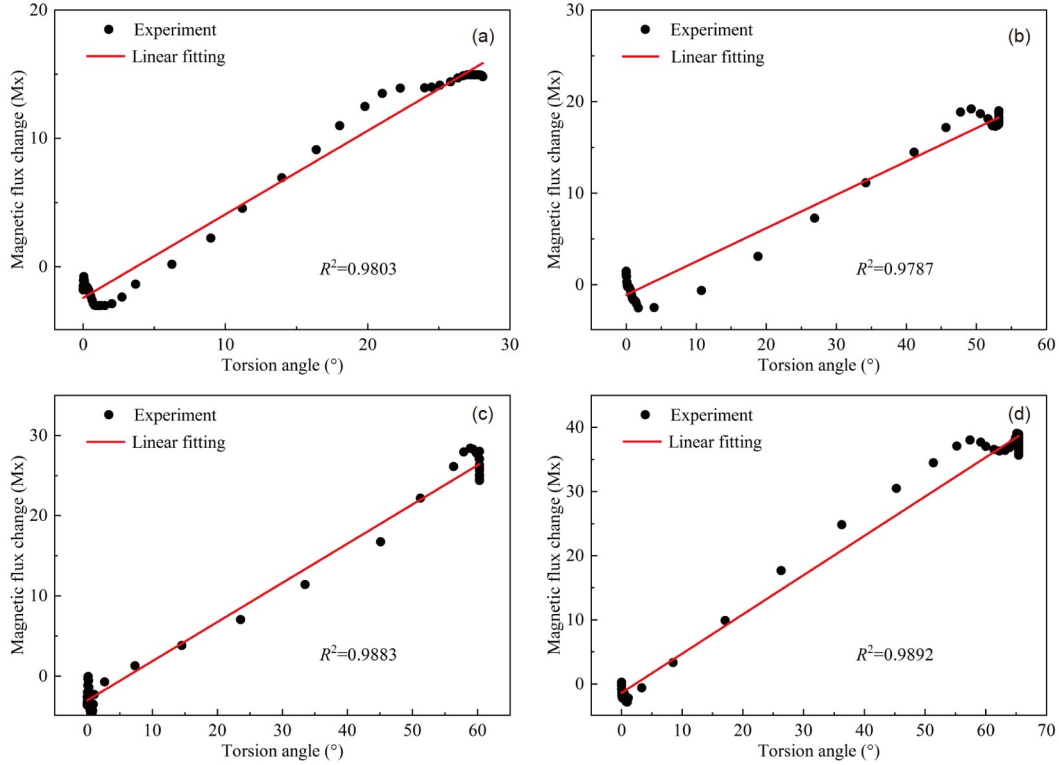
Figure 9 (Color online) Relationship between the magnetic flux change and the torsion angle of the SPTA for the actuating pressures of (a) −10 kPa, (b) −20 kPa, (c) −30 kPa, and (d) −40 kPa.

relationship between the magnetic flux change and the torsion angle of the SPTA.

3.3   Calibration on the feedback signal

The calibration of the feedback signal is important for the application of the SPTA. In this section, the nonlinearity and sensitivity of the feedback signal for the SPTA are discussed. The measure experiments are conducted at room temperature (about 25°C±3°C). The experimental data are displayed in Figure 10. To obtain the nonlinearity and sensitivity, the least square method is employed to fit the experimental data. The sensitivity S and nonlinearity δ_L can be calculated by eqs. (6) and (7), respectively.

$$S = \frac{\Delta y}{\Delta x}, \tag{6}$$

$$\delta_L = \frac{B_{\max}}{A} \times 100\%, \tag{7}$$

where Δy is the change of magnetic flux change due to a micro-increment of torsion angle Δx, $B_{\max}$ is the maximum deviation between the experiment data and the fitting line, and A is the variation range of the magnetic flux change. Here, the average sensitivity and nonlinearity are obtained, which are 0.560 Mx/° and 16.6%. In short, these indicators are both in an acceptable range, but also need to be improved further.
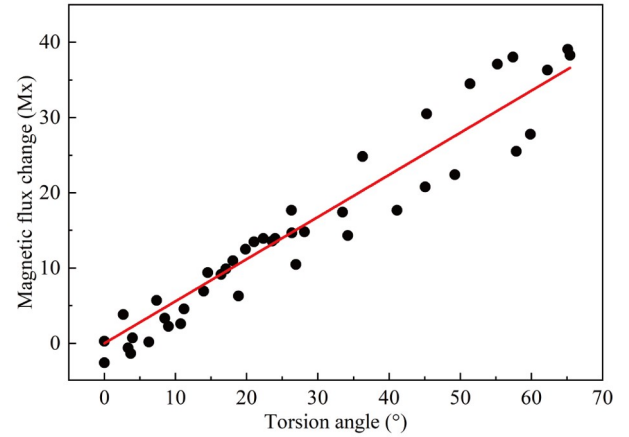

Figure 10 (Color online) Experimental data of the torsion angle and magnetic flux change.

3.4   Effect of parameters on the electrical characteristics

The electrical characteristics are an important feature for the SPTA. Herein, the effect of different parameters on the electrical characteristics, including the feedback voltage and current, is investigated experimentally. According to eq. (1), the number of turns of the varnished wire can affect the electrical characteristics. And based on Faraday's electromagnetic induction laws, eq. (1) can be also rewritten into:

$$E(v) = -N \cdot \frac{\Delta \Phi}{\Delta t} = -N \cdot \frac{\Delta B \cdot S}{\Delta t}, \tag{8}$$

where B is the magnetic intensity, S is the area of the wire that is perpendicular to B. Hence, magnetic intensity plays a significant role in electrical characteristics. For this structure design, the addition of magnetic powders is essential for the self-sensing ability of the SPTA. And the content of magnetic powders will directly influence the magnetic intensity of the local magnetic field. In addition, the magnetic direction of the SPTA may also affect the electrical characteristics. Therefore, the effect of the three factors is studied experimentally in the section.

Firstly, the effect of the number of turns of the varnished wire is studied experimentally. Before experiments, we prepared three SPTAs with 25, 50, and 75 turns (mass fractions of magnetic powders is 50%). And measurements are conducted to obtain the electrical characteristics. During the measurements, the SPTAs are actuated by a pressure of −40 kPa, and then recover as the pressure is released. Figure 11 displays the feedback voltage and current within five cycles and their average maximum for the five cycles. For the cycles, the feedback voltage and current exhibit repeatability and consistency. The slight distinction is mainly due to the noise signal during the measurements. From Figure 11, we can also discover that the feedback signal of the torsion process is bigger than that of the recovery process. With the rise of the number of turns, the feedback voltage and current both increase. As regards the torsion process, the maximum feedback voltage increases from 2.45 to 4.06 μV while the maximum feedback current changes from 25.72 to 37.77 nA.

Secondly, the influence of the content of magnetic powders on the electrical characteristics of the SPTA is discussed.

Three SPTAs with the magnetic powders content of 30 wt%, 40 wt%, and 50 wt% were fabricated. The magnetic intensity of the finished SPTA is studied before conducting the measurement of the feedback signal. Here, the WT10A Teslameter (WEITE Magnetic Technology Co., Ltd, China) is used to test the magnetic intensity. The magnetic intensities of the SPTAs with the mass fraction of 30 wt%, 40 wt%, and 50 wt% are 12.05, 19.50, and 30.40 mT, respectively. Then, the feedback voltage and current are obtained by the multimeter, and their variation with respect to time is plotted in Figure 12. Expectedly, the increase of magnetic powders will enhance the feedback voltage and current. And results show that the maximum feedback voltage rises from 2.26 to 2.90 μV (torsion process) when the magnetic powders content varies from 30 wt% to 50 wt%. For the maximum feedback current, it increases from 21.52 to 29.50 nA.

Finally, we explore the effect of the magnetic direction of the SPTA on the feedback voltage and current. In general, the magnetic direction of the SPTA can be arbitrary. In this study, we only consider two typical cases, including the directions that are parallel to and perpendicular to the length direction of the helical wire. Two SPTAs with the same parameters (magnetic powders content is 50 wt%, 50 turns) were fabricated, while the magnetic direction is different. The feedback voltage and current for the two SPTAs were tested, as depicted in Figure 13. The experimental results demonstrate that the magnetic direction parallel to the length direction of the helical wire has slight advantages in improving the feedback voltage and current. For the magnetic direction parallel to the length direction of the helical wire, the maximum feedback voltage and current are 2.90 μV and 29.50 nA during the actuating process. Whereas, the max-
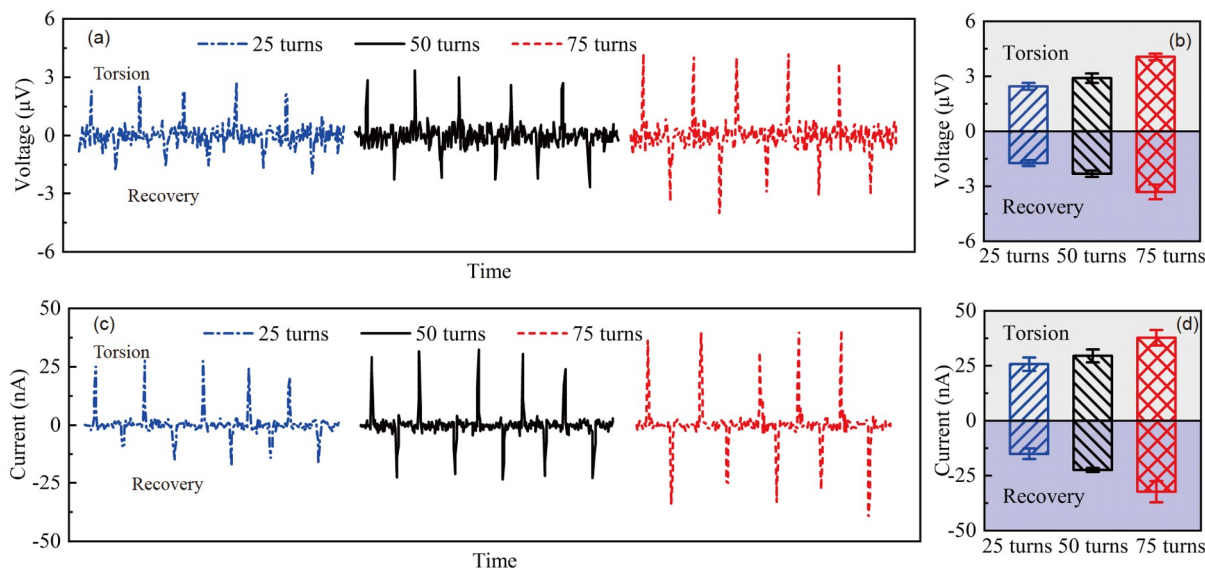

Figure 11 (Color online) Effect of the number of turns of the varnished wire on the electrical characteristics of the SPTA. (a) Feedback voltage versus time curves; (b) maximum feedback voltage; (c) feedback current versus time curves; (d) maximum feedback current.

Figure 12 (Color online) Effect of the mass fraction of magnetic particles on the electrical characteristics of the SPTA. (a) Feedback voltage versus time curves; (b) maximum feedback voltage; (c) feedback current versus time curves; (d) maximum feedback current.

Figure 13 (Color online) Effect of magnetic direction on the electrical characteristics of the SPTA. (a) Feedback voltage versus time curves; (b) maximum feedback voltage; (c) feedback current versus time curves; (d) maximum feedback current.
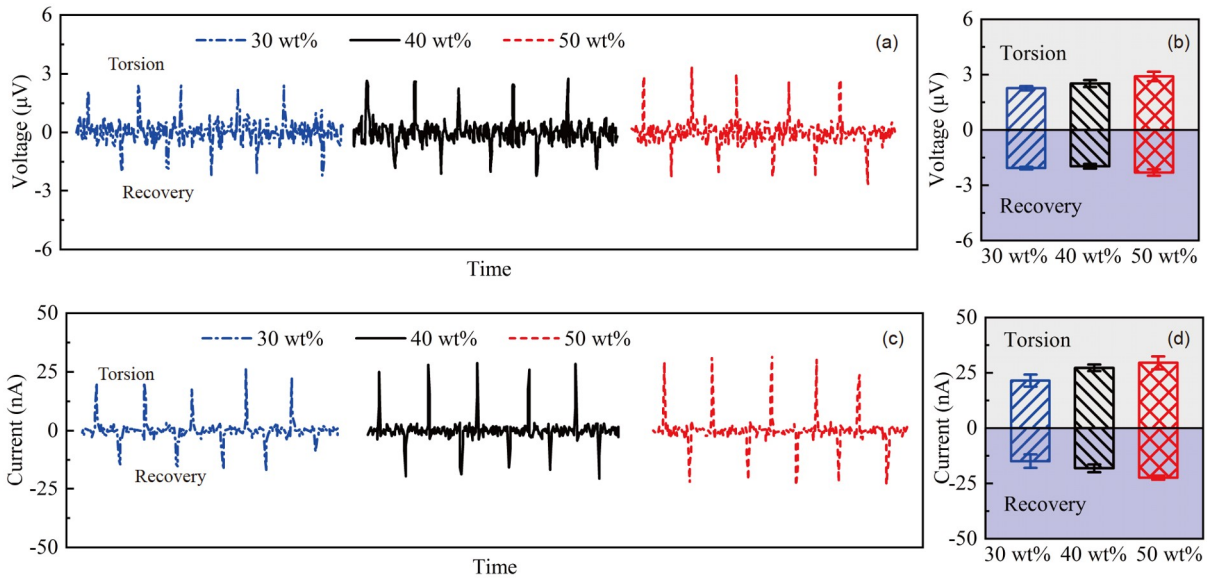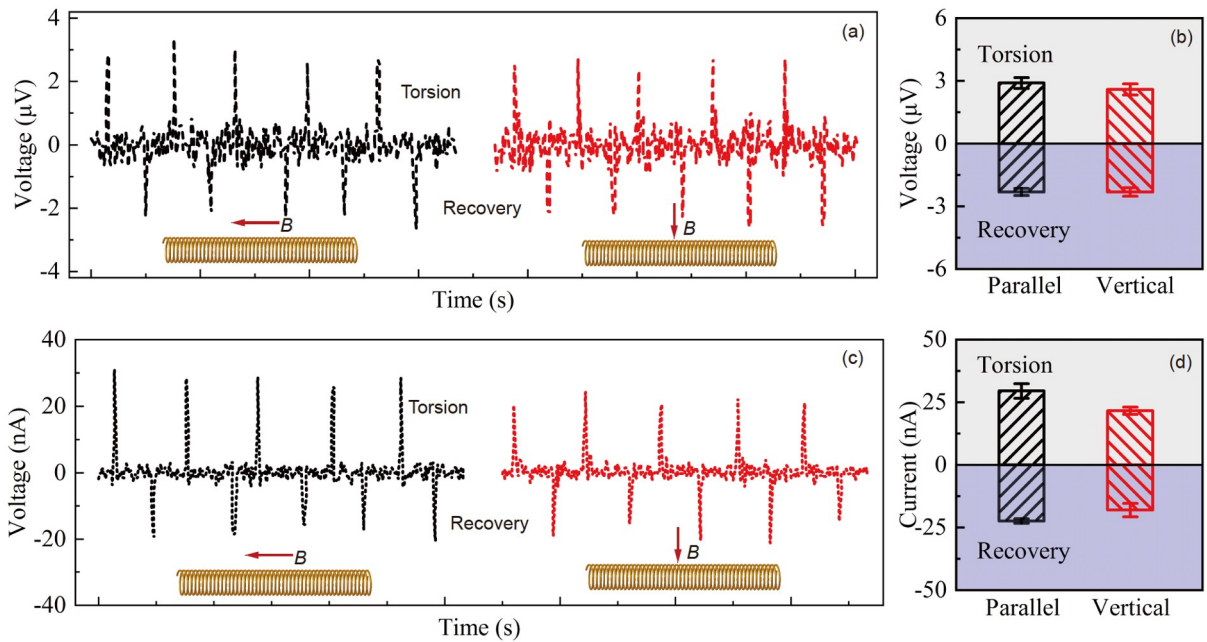
imum feedback voltage and current are 2.59 µV and 21.66 nA for another case.

For the SPTAs with different parameters, their resistance is summarized in Table 1. The resistance merely depends on the length of the varnished wire. Thus, the resistance rises with the increasing number of turns, while that of the SPTAs with different magnetic powder contents is almost the same. Note that the resistance of SPTAs is almost unchanged as the

SPTAs are deformed under depressurization.

In short, the number of turns can improve the feedback voltage and current of the SPTA. The maximum number of turns relies on the diameter of enameled wires and the height of the torsion actuator. Thus, the growth of the feedback voltage and current via increasing the number of turns is limited. Additionally, the magnetic powder contents are capable of enhancing the feedback electrical signal. On the

Table 1   Resistance of the SPTAs with different parameters

Parameter		Resistance (Ω)
Different turns	25 turns	0.3725
	50 turns	0.5351
	75 turns	0.7302
Magnetic powder contents	30 wt%	0.5527
	40 wt%	0.5524
	50 wt%	0.5451
Magnetic direction	Parallel	0.5351
	Vertical	0.5432

other hand, the higher content of magnetic powders means that there is less silicone rubber to connect the magnetic powders. So the silicone rubber/NdFeB composite is more prone to breakage under external loads and is difficult to cure.

4   Discussion

So far, many soft sensors with high compliance and extensibility are designed and fabricated. These sensors can be a candidate for the sensing of soft robots. However, there is indeed a technological gap to readily embed them into soft robots and then effectively sense the deformation of soft robots. Herein, we proposed a self-sensing pneumatic torsional actuator having some advantages that make it attractive in soft robots. Firstly, the SPTA is completely soft though the magnetic powder and varnished wire are hard. And the numerical results show that the addition of the magnetic powder and varnished wire has a slight effect on the torsional actuator deformation, while they can enhance the output torque of the torsional actuator. Secondly, the fabrication of the SPTA is pretty simple, which only needs to put the helical wire into the molds before pouring the composite. Thirdly, the perception of our developed SPTA originates from the actuator architecture. Whereas other self-sensing actuators [31,51,52] need to take the installation and arrangement of sensing elements into account. Importantly, the sensing mechanism is effective, and can be applied to other soft actuators, such as fiber-reinforced bending actuators [53,54], pneu-net actuators [55,56], and origami-inspired actuators [57,58].

On the other hand, there are some negative effects of the integration of the copper wires and NdFeB magnetic powders on the actuator. Firstly, the fabrication is more complicated compared with the actuator fabricated by pure rubber E625. Secondly, the fluidity of silicone rubber/NdFeB composite is reduced with the rise of magnetic powder contents, which will increase the difficulty of fabrication. When the magnetic powder content is up to 70%, the fabrication fails because of the poor fluidity. Thirdly, the in-

tegration of the copper wires and NdFeB magnetic powders leads to an increase in the torsion stiffness, which means a bigger actuating pressure is needed.

In conclusion, this work mainly reveals the mechanical and electrical characteristics of the SPTA, which is fundamental for intelligent soft robots. To realize the accuracy control and intelligentization of soft robots, our future work will focus on dynamics modeling, control algorithm developing and robust controller constructing.

5   Conclusion

In this study, we have proposed a self-sensing pneumatic torsional actuator, which only contains an elastomeric body made by silicone rubber/NdFeB composite and a helical varnished wire placed in the body. The sensing capacity originates from the inherent structure of the SPTA. So the SPTA feels its torsion deformation without redundant sensors as the actuator is actuated by different pressures. Firstly, the mechanical characteristics of the SPTA are studied experimentally and numerically. The experimental results demonstrate that the developed FEM is effective in predicting the mechanical characteristics of the SPTA. On the basis of the FEM, we discuss the torsion performance of the actuators fabricated by pure rubber, silicone rubber/NdFeB composite, and silicone rubber/NdFeB composite and helical varnished wire, respectively. The FEM results show that the maximum torsion angle and output torque of the SPTA are about 66.35° and 25.07 N mm. Compared with the torsional actuator fabricated by pure rubber, the maximum torsion angle of the SPTA is reduced by 15.68% while the maximum output torque is enhanced by 23.19%. Then, we reveal the electrical characteristics of the SPTA as step signals with different pressure amplitudes are applied to the helical chambers. The torsion deformation of the SPTA increases with the rise of pressure amplitudes, resulting in the growth of the feedback voltage. According to the experimental data, we disclose the relationship between the magnetic flux and the deformation of the SPTA. The values of R^2 for different pressure amplitudes are all over 0.95, which demonstrates that the magnetic flux change and the torsion angle exhibit a strong linear correlation. Finally, we reveal the effect of the number of turns of the varnished wire, magnetic powders contents, and magnetic direction on the feedback voltage and current. The feedback voltage and current can be enhanced by increasing the number of turns and magnetic powders contents, while they are insensitive to the magnetic direction of the SPTA. In conclusion, these findings are fundamental for us to understand the mechanical and electrical characteristics of the SPTA. And we believe that the SPTA will possess promising applications in the future, especially for unconstructed environments.

1 Luo X, Xie F, Liu X J, et al. Kinematic calibration of a 5-axis parallel machining robot based on dimensionless error mapping matrix. Rob Comput Integr Manuf, 2021, 70: 102115

2 Wu J, Song Y Y, Liu Z L, et al. A modified similitude analysis method for the electro-mechanical performances of a parallel manipulator to solve the control period mismatch problem. Sci China Tech Sci, 2022, 65: 541–552

3 Wu J, Yu G, Gao Y, et al. Mechatronics modeling and vibration analysis of a 2-DOF parallel manipulator in a 5-DOF hybrid machine tool. Mech Mach Theory, 2018, 121: 430–445

4 Rus D, Tolley M T. Design, fabrication and control of soft robots. Nature, 2015, 521: 467–475

5 Calisti M, Giorelli M, Levy G, et al. An octopus-bioinspired solution to movement and manipulation for soft robots. Bioinspir Biomim, 2011, 6: 036002

6 Odhner L U, Dollar A M. Stable, open-loop precision manipulation with underactuated hands. Int J Robotics Res, 2015, 34: 1347–1360

7 Miriyev A, Stack K, Lipson H. Soft material for soft actuators. Nat Commun, 2017, 8: 1–8

8 Li X, Duan H, Lv P, et al. Soft actuators based on liquid-vapor phase change composites. Soft Robotics, 2021, 8: 251–261

9 Wani O M, Zeng H, Priimagi A. A light-driven artificial flytrap. Nat Commun, 2017, 8: 15546

10 Zou J, Feng M, Ding N, et al. Muscle-fiber array inspired, multiple-mode, pneumatic artificial muscles through planar design and one-step rolling fabrication. Natl Sci Rev, 2021, 8: nwab048

11 Gong Z, Fang X, Chen X, et al. A soft manipulator for efficient delicate grasping in shallow water: Modeling, control, and real-world experiments. Int J Robotics Res, 2021, 40: 449–469

12 Xiao W, Hu D, Yang G, et al. Modeling and analysis of soft robotic surfaces actuated by pneumatic network bending actuators. Smart Mater Struct, 2022, 31: 055001

13 Hao Y, Gong Z, Xie Z, et al. A soft bionic gripper with variable effective length. J Bionic Eng, 2018, 15: 220–235

14 Xiao W, Liu C, Hu D, et al. Soft robotic surface enhances the grasping adaptability and reliability of pneumatic grippers. Int J Mech Sci, 2022, 219: 107094

15 Gu G, Zhang N, Xu H, et al. A soft neuroprosthetic hand providing simultaneous myoelectric control and tactile feedback. Nat Biomed Eng, 2023, 7: 589–598

16 Zhang N B, Zhao Y, Gu G Y, et al. Synergistic control of soft robotic hands for human-like grasp postures. Sci China Tech Sci, 2022, 65: 553–568

17 Marchese A D, Onal C D, Rus D. Autonomous soft robotic fish capable of escape maneuvers using fluidic elastomer actuators. Soft Robotics, 2014, 1: 75–87

18 Wu M, Zheng X, Liu R, et al. Glowing sucker octopus (*stauroteuthis syrtensis*)-inspired soft robotic gripper for underwater self-adaptive grasping and sensing. Adv Sci, 2022, 9: 2104382

19 Yamamoto T, Sakama S, Kamimura A. Pneumatic duplex-chambered inchworm mechanism for narrow pipes driven by only two air supply lines. IEEE Robot Autom Lett, 2020, 5: 5034–5042

20 Ball E J, Meller M A, Chipka J B, et al. Modeling and testing of a knitted-sleeve fluidic artificial muscle. Smart Mater Struct, 2016, 25: 115024

21 Yang D, Verma M S, So J, et al. Buckling pneumatic linear actuators inspired by muscle. Adv Mater Technologies, 2016, 1: 1600055

22 Oguntosin V, Akindele A. Design and characterization of artificial muscles from wedge-like pneumatic soft modules. Sens Actuat A-Phys, 2019, 297: 111523

23 Xiao W, Hu D, Chen W, et al. Design, characterization and optimization of multi-directional bending pneumatic artificial muscles. J

24 Zhu J Q, Pu M H, Chen H, et al. Pneumatic and tendon actuation coupled muti-mode actuators for soft robots with broad force and speed range. Sci China Tech Sci, 2022, 65: 2156–2169

25 Pan Q, Chen S T, Chen F F, et al. Programmable soft bending actuators with auxetic metamaterials. Sci China Tech Sci, 2020, 63: 2518–2526

26 Gong X, Yang K, Xie J, et al. Rotary actuators based on pneumatically driven elastomeric structures. Adv Mater, 2016, 28: 7533–7538

27 Yang D, Mosadegh B, Ainla A, et al. Buckling of elastomeric beams enables actuation of soft machines. Adv Mater, 2015, 27: 6323–6327

28 Jiao Z, Ji C, Zou J, et al. Vacuum-powered soft pneumatic twisting actuators to empower new capabilities for soft robots. Adv Mater Technologies, 2019, 4: 1800429

29 Xiao W, Du X, Chen W, et al. Cooperative collapse of helical structure enables the actuation of twisting pneumatic artificial muscle. Int J Mech Sci, 2021, 201: 106483

30 Li S, Zhao H, Shepherd R F. Flexible and stretchable sensors for fluidic elastomer actuated soft robots. MRS Bull, 2017, 42: 138–142

31 Ying B, Chen R Z, Zuo R, et al. An anti-freezing, ambient-stable and highly stretchable ionic skin with strong surface adhesion for wearable sensing and soft robotics. Adv Funct Mater, 2021, 31: 2104665

32 Wang D, Zhang J, Ma G, et al. A selective-response bioinspired strain sensor using viscoelastic material as middle layer. ACS Nano, 2021, 15: 19629–19639

33 Lo L W, Zhao J, Wan H, et al. A soft sponge sensor for multimodal sensing and distinguishing of pressure, strain, and temperature. ACS Appl Mater Interfaces, 2022, 14: 9570–9578

34 Wan Y, Qiu Z, Huang J, et al. Natural plant materials as dielectric layer for highly sensitive flexible electronic skin. Small, 2018, 14: 1801657

35 Zhou L Y, Gao Q, Zhan J F, et al. Three-dimensional printed wearable sensors with liquid metals for detecting the pose of snakelike soft robots. ACS Appl Mater Interfaces, 2018, 10: 23208–23217

36 Li Z, Cheng L, Liu Z. Intentional blocking based photoelectric soft pressure sensor with high sensitivity and stability. Soft Robotics, 2023, 10: 205–216

37 Ilami M, Bagheri H, Ahmed R, et al. Materials, actuators, and sensors for soft bioinspired robots. Adv Mater, 2020, 33: 2003139

38 Jiao Z D, Ye Z Q, Zhu P A, et al. Self-sensing actuators with programmable actuation performances for soft robots. Sci China Tech Sci, 2023, 66: 3070–3079

39 Kanno R, Watanabe S, Shimizu K, et al. Self-sensing McKibben artificial muscles embedded with dielectric elastomer sensor. IEEE Robot Autom Lett, 2021, 6: 6274–6280

40 Truby R L, Wehner M, Grosskopf A K, et al. Soft somatosensitive actuators via embedded 3D printing. Adv Mater, 2018, 30: 1706383

41 Zhao H, O'Brien K, Li S, et al. Optoelectronically innervated soft prosthetic hand via stretchable optical waveguides. Sci Robot, 2016, 1: i7529

42 Chen W, Xiong C, Liu C, et al. Fabrication and dynamic modeling of bidirectional bending soft actuator integrated with optical waveguide curvature sensor. Soft Robotics, 2019, 6: 495–506

43 Tawk C, Alici G. A review of 3D-printable soft pneumatic actuators and sensors: Research challenges and opportunities. Adv Intelligent Syst, 2021, 3: 2000223

44 Wang H, Totaro M, Beccai L. Toward perceptive soft robots: Progress and challenges. Adv Sci, 2018, 5: 1800541

45 Rome L C, Flynn L, Goldman E M, et al. Generating electricity while walking with loads. Science, 2005, 309: 1725–1728

46 Hu W, Lum G Z, Mastrangeli M, et al. Small-scale soft-bodied robot with multimodal locomotion. Nature, 2018, 554: 81–85

47 Kim Y, Yuk H, Zhao R, et al. Printing ferromagnetic domains for untethered fast-transforming soft materials. Nature, 2018, 558: 274–279

48 Xiao W, Hu D, Chen W, et al. A new type of soft pneumatic torsional actuator with helical chambers for flexible machines. J Mech Ro-

Bionic Eng, 2021, 18: 1358–1368

botics, 2021, 13: 11003

49   Xiao W, Hu D, Zhou H, et al. A self-sensing intelligent soft pneumatic actuator with soft magnetic structures. Int J Mech Sci, 2023, 250: 108279

50   Yeoh O H. Some forms of the strain energy function for rubber. Rubber Chem Tech, 1993, 66: 754–771

51   Yang H, Chen Y, Sun Y, et al. A novel pneumatic soft sensor for measuring contact force and curvature of a soft gripper. Sens Actuat A-Phys, 2017, 266: 318–327

52   Ho V, Hirai S. Design and analysis of a soft-fingered hand with contact feedback. IEEE Robot Autom Lett, 2017, 2: 491–498

53   Sun Y, Feng H, Manchester I R, et al. Static modeling of the fiber-reinforced soft pneumatic actuators including inner compression: Bending in free space, block force, and deflection upon block force.

Soft Robotics, 2022, 9: 451–472

54   Polygerinos P, Wang Z, Overvelde J T B, et al. Modeling of soft fiber-reinforced bending actuators. IEEE Trans Robot, 2015, 31: 778–789

55   Gu G, Wang D, Ge L, et al. Analytical modeling and design of generalized pneu-net soft actuators with three-dimensional deformations. Soft Robotics, 2021, 8: 462–477

56   Xiao W, Hu D, Chen W, et al. Modeling and analysis of bending pneumatic artificial muscle with multi-degree of freedom. Smart Mater Struct, 2021, 30: 095018

57   Jiao Z, Zhang C, Ruan J, et al. Re-foldable origami-inspired bidirectional twisting of artificial muscles reproduces biological motion. Cell Rep Phys Sci, 2021, 2: 100407

58   Kim W, Byun J, Kim J K, et al. Bioinspired dual-morphing stretchable origami. Sci Robot, 2019, 4: y3493